Geotech Geol Eng (2018) 36:3583–3600
https://doi.org/10.1007/s10706-018-0559-y

ORIGINAL PAPER

Seismic Stability of a Tunnel Considering the Dynamic Geologic Parameters of Loess

Xuansheng Cheng · Xinlei Li · Jin Fan · Guoliang Li

Received: 23 October 2017 / Accepted: 25 April 2018 / Published online: 7 May 2018

Abstract In this study, Taiyuan loess is used in the analysis of the seismic stability of a loess tunnel. This analysis considers the dynamic parameters of the loess as determined via triaxial compression tests in the literature. In this analysis, the consolidation pressure is converted into the thickness of the overlying loess layer. The spring stiffness and damping coefficients of the viscoelastic boundary are obtained using the maximum dynamic elastic modulus in conjunction with different loess moisture contents and Poisson's ratios. Additionally, the loess cohesion and internal friction angle are also obtained for different moisture contents. By (1) utilizing the dynamic finite element static shear strength reduction method and the non-convergence rule, (2) taking the safety factor as the assessment standard for loess tunnel stability, and (3) reducing the dynamic parameters of the loess mass until the model calculation is non-convergent, the effects of the moisture content, seismic intensity and loess thickness on the safety factor are obtained. A theoretical basis for the seismic response analysis of this type of loess tunnel is provided by considering the dynamic parameters of loess.

Keywords Loess · Tunnel · Earthquake · Dynamic parameters · Stability

1 Introduction

Dynamic parameters can greatly influence the stability of a loess tunnel. Earthquakes can damage loess tunnels by disturbing the loess and changing the loess characteristics, and damaged tunnels are difficult and expensive to repair. Thus, it is important and meaningful to study the seismic stability of loess tunnels. Many tunnel collapses, large deformation events and other safety accidents occur because the stability of the loess mass surrounding the tunnel does not meet the required standards. Therefore, the stress characteristics, stability and early deformation warning indicators of the loess surrounding a tunnel need to be urgently studied.

In recent years, scholars have performed considerable research on the stability of loess tunnels, and these studies have focused on the influence of different factors on the stability of loess tunnels. Peila (1994)

X. Cheng (✉) · X. Li · J. Fan · G. Li
Key Laboratory of Disaster Prevention and Mitigation in Civil Engineering of Gansu Province, Lanzhou University of Technology, Lanzhou 730050, People's Republic of China
e-mail: chengxuansheng@gmail.com

X. Cheng · X. Li · J. Fan · G. Li
Western Engineering Research Center of Disaster Mitigation in Civil Engineering of Ministry of Education, Lanzhou University of Technology, Lanzhou 730050, People's Republic of China

conducted a theoretical study on the stability of a tunnel section. Yang and Chang (2000) performed a calculation and analysis of the stability of a rock mass during the construction process of a large group of caverns by combining specific examples of hydropower stations. Zheng et al. (2008) proposed using the safety coefficient calculated by the strength reduction finite element method as the basis for judging the stability of a tunnel. In addition, loess tunnels have been used as examples for determining the shear safety factor and the tensile safety factor. Li et al. (2011) analyzed unsaturated loess slope stabilities using a program developed on the basis of the strength reduction finite element method. (Griffiths and Lane 1999; Dawson et al. 1999) performed a stability analysis of a slope using the strength reduction method. Zheng et al. (2002) reduced the shear strength of the finite element model to obtain the safety factor of a slope. (Soranzo et al. 2015) studied the face stability of shallow tunnels in partially saturated soil. Chen et al. (2011) analyzed the ultimate displacement values of rock in a tunnel and proposed using acceleration to determine the stability of the rock surrounding a tunnel. Xu (2005) analyzed and evaluated the stability of tunnels from a qualitative point of view and noted seismic measures that require attention in tunnel design and construction. Zhang et al. (2007) calculated the safety factor and potential slip surface by analyzing the seismic stability of a tunnel. Qiu et al. (2009) analyzed the failure mechanism of a loess tunnel and proposed two safety coefficient concepts related to tunnel stability: shearing and cracking. Guo and Wang (2011) analyzed the dynamic construction process of the Xin Baotashan tunnel, which is surrounded by grade IV rock. Zhang et al. (2009) proposed requirements for loess tunnel stability. With the development of computer technology, many new methods have been developed to analyze the stability analysis of loess tunnels, and the stability analysis of loess tunnels includes both static analysis and dynamic analysis. Cheng et al. (2010, 2014) proposed two new methods using the seismic safety coefficient to evaluate the seismic stability of tunnels. Zheng et al. (2010) proposed a static finite element analysis and two dynamic analysis methods on the basis of the static analysis of the loess tunnel lining, and the methods considered tensional failure and compressional failure. Zheng et al. (2010) proposed a new dynamic analysis method based on the finite element strength reduction method. Cheng et al. (2011a, b), (2017), Cheng and Zheng (2011), conducted static and dynamic stability tests in a loess tunnel with a large span and an egg-shaped cross section; the results show that the loess tunnel span, soil thickness and seismic intensity affect the safety factor and stability. From an energy perspective, Zhang et al. (2015) researched seismic effects on the stability of shallowly buried loess tunnels using a pseudo-static method. Liu et al. (2012) used 3 multi-parameter growth functions (i.e., the Weibull growth function, Richard function and Gompertz growth function) and 3 kinds of commonly used functions (i.e., exponential, logarithmic and hyperbolic functions) to conduct a regression analysis of the initial structure of a loess tunnel in northwestern China.

In summary, although theoretical derivation and numerical simulation methods have been used to perform seismic stability analysis of loess tunnels in the existing literature, the loess parameters have been determined based on static parameters in the analysis and calculation process. To conduct a more accurate seismic stability analysis of loess tunnels in this paper, previous experimental results are summarized, and the consolidation pressure is converted into the overlying loess layer thickness. By utilizing the maximum dynamic elastic modulus and Poisson's ratio of loess with different moisture contents, the spring stiffness and damping coefficient of the viscoelastic boundary are calculated. Using the dynamic finite element static strength reduction method, the dynamic seismic stability of the loess tunnel is studied. With consideration of the effects of different loess cover thicknesses and moisture contents on the safety coefficient and plastic zone of loess tunnels under the effects of an earthquake, the loess tunnel failure mechanism is determined, and the results used to guide the design and construction of loess tunnels.

2 Calculation Method

2.1 Strength Reduction Method

When the initial moisture content of the original loess is greater than the liquid limit but smaller than the plastic limit, the corresponding strength is controlled by the shear strength of the soil (which is dependent on the cohesion and internal friction angle) (Zhou et al. 2001). Considering that the most detrimental state is when the initial moisture content of the soil is greater than the plastic limit, the Coulomb theory is used to calculate the shear strength, i.e., $\tau = c + \sigma \tan \varphi$.

Zienkiewicz et al. (1975) first proposed the concept of the shear strength reduction factor. The safety factor is consistent with the safety factor given by Bishop. The basic concept of the strength reduction method involves keeping the gravitational acceleration of the soil constant and dividing both shear strength parameters (cohesion and internal friction angle) by a reduction factor η, as shown in Eqs. (1) and (2) in the reduced form. Then, the reduced virtual shear strength parameters (cohesion c_f and internal friction angle φ_f) replace the shear strength parameters in the original equation, as shown in Eq. (3), which is used to calculate the new material parameters. The calculation and analysis are performed repeatedly, and the reduction coefficient η is increased until the structure reaches the critical failure state. The resulting reduction factor is the safety factor.

$$c_f = \frac{c}{\eta} \tag{1}$$

$$\phi_f = \arctan\left(\frac{\tan \phi}{\eta}\right) \tag{2}$$

$$\tau_f = c_f + \sigma \tan \varphi_f \tag{3}$$

where c_f is the reduced fictitious cohesive strength of the soil; φ_f is the reduced fictitious internal friction angle; and τ_f is the reduced shear strength.

To ensure that the initial problem is almost elastic, the initial value of the reduction factor should be sufficiently small. Then, by increasing the reduction coefficient, the shear strength gradually decreases after reduction until it reaches the critical failure state. At this point, the corresponding reduction coefficient is the stability safety coefficient.

2.2 Failure Criterion

Among the judgment criteria for the critical state of damage in the existing literature (Zienkiewicz et al. 1975), the results of the non-convergence criterion are more conservative than the results of the feature point displacement criterion, the criterion of the surrounding rock in the plastic zone, and the lining and anchor yield criterion. Therefore, in this paper, the non-convergence criterion of the calculation is chosen as the stability criterion for the loess tunnel.

The non-convergence criterion of the calculation confirms whether the calculation process of the structural simulation is convergent. For a given convergence criterion, if the numerical calculation process is convergent, the structure is in a steady state. If the numerical calculation is not convergent, the structure is damaged, and at this point, the reduction factor is the safety factor.

2.3 Displacement Calculation

Under earthquake conditions, the differential equation (Chen et al. 2007; Peng et al. 2008) is

$$\mathrm{M}\ddot{\mathbf{u}}(\mathrm{t}) + \mathrm{C}\dot{\mathbf{u}}(\mathrm{t}) + \mathrm{Ku}(\mathrm{t}) = -\mathrm{M}\ddot{\mathbf{u}}_{\mathrm{g}}(\mathrm{t}) + \mathbf{p}_{\mathrm{f}} \tag{4}$$

where **C**, **M** and **K** are the damping matrix, mass matrix, and stiffness matrix, respectively. The terms $\ddot{\mathbf{u}}(t)$, $\dot{\mathbf{u}}(t)$ and $\mathbf{u}(t)$ are the acceleration, velocity, and displacement vector of the model node, respectively. Additionally, $\ddot{\mathbf{u}}_{\mathrm{g}}$ is the earthquake acceleration, and $\mathbf{p}_{\mathrm{f}}$ is the vector of the surface load.

The Newmark-β method is used to solve the matrix differential equation, as follows:

$$\mathbf{u}_{\mathrm{t}+\Delta\mathrm{t}} = \mathbf{u}_{\mathrm{t}} + \Delta\mathrm{t}\underline{\mathbf{u}}_{\mathrm{t}} + \left(\frac{1}{2} - \varsigma\right)\Delta\mathrm{t}^2\dot{\mathbf{u}}_{\mathrm{t}} + \varsigma\Delta\mathrm{t}^2\ddot{\mathbf{u}}_{\mathrm{t}+\Delta\mathrm{t}} \tag{5}$$

$$\dot{\mathbf{u}}_{\mathrm{t}+\Delta\mathrm{t}} = \dot{\mathbf{u}}_{\mathrm{t}} + (1-\tau)\Delta t\ddot{u}_{\mathrm{t}} + \tau\Delta t\ddot{u}_{\mathrm{t}+\Delta\mathrm{t}} \tag{6}$$

where τ and ς are constants.

The motion differential equation at time t + Δt is

Table 1 Calculation parameters for the viscoelastic boundary

Water content (%)	Confining pressure (MPa)	Normal spring stiffness K_{BN} (N/m)	Normal damping coefficient C_{BN} (N s/m)	Tangential spring stiffness K_{BT} (N/m)	Tangential damping coefficient C_{BT} (N s/m)
5	100	3.025E+5	3.257E+4	1.512E+5	1.565E+4
	150	4.454E+5	3.953E+4	2.227E+5	1.899E+4
	200	9.437E+5	5.754E+4	4.718E+5	2.764E+4
10	100	2.554E+5	2.993E+4	1.277E+5	1.438E+4
	150	2.794E+5	3.111E+4	1.397E+5	1.495E+4
	200	3.458E+5	3.483E+4	1.729E+5	1.673E+4
15	100	1.976E+5	2.633E+4	9.88E+4	1.265E+4
	150	2.141E+5	2.741E+4	1.071E+5	1.316E+4
	200	2.348E+5	2.870E+4	1.174E+5	1.379E+4

$$M\ddot{\mathbf{u}}_{t+\Delta t} + C\dot{\mathbf{u}}_{t+\Delta t} + K\mathbf{u}_{t+\Delta t} = -M\ddot{\mathbf{u}}_{g(t+\Delta t)} + \mathbf{p}_f \quad (7)$$

With regards to the basic parameters, the Newmark-β method is absolutely stable for values of $\tau = 0.5$, $\varsigma = 0.25$ and $\Delta t \leq \frac{T_{\max}}{100}$, and the result reaches the required accuracy.

Substituting Eqs. (5) and (6) into Eq. (7) results in

$$\left(\mathbf{M} + \frac{\Delta t}{2}\mathbf{C}\right)\dot{\mathbf{u}}_{t+\Delta t} + \mathbf{C}\left(\dot{\mathbf{u}}_t + \frac{\Delta t}{2}\dot{\mathbf{u}}_t\right) + \mathbf{K}\mathbf{u}_{t+\Delta t} = -\mathbf{M}\mathbf{u}_{g(t+\Delta t)} + \mathbf{p}_f \quad (8)$$

From Eq. (6), the following is obtained:

$$\ddot{\mathbf{u}}_{t+\Delta t} = \frac{4}{\Delta t^2}(\mathbf{u}_{t+\Delta t} - \mathbf{u}_t) - \frac{4}{\Delta t}\dot{\mathbf{u}}_t - \ddot{\mathbf{u}}_t \quad (9)$$

Substituting Eqs. (9) into (8) produces

$$\left(\mathbf{K} + \frac{2}{\Delta t}\mathbf{C} + \frac{4}{\Delta t^2}\mathbf{M}\right)\mathbf{u}_{t+\Delta t} = \mathbf{C}\left(\frac{2}{\Delta t}\mathbf{u}_t + \dot{\mathbf{u}}_t\right) + \mathbf{M}\left(\frac{4}{\Delta t^2}\mathbf{u}_t + \frac{4}{\Delta t}\dot{\mathbf{u}}_t + \ddot{\mathbf{u}}_t\right) - \mathbf{M}\ddot{\mathbf{u}}_{g(t+\Delta t)} + \mathbf{p}_f \quad (10)$$

$\mathbf{u}_{t+\Delta t}$ can be obtained from Eq. (10), and $\ddot{\mathbf{u}}_{t+\Delta t}$ and $\dot{\mathbf{u}}_{t+\Delta t}$ can be obtained from Eqs. (9) and (6), respectively.

3 Boundary Conditions and Seismic Waves

3.1 Boundary Conditions

The viscoelastic boundary can overcome the problem of low-frequency drift caused by a viscous boundary, and it has better frequency stability, accuracy and convergence displacement. Absorption of the scattering wave is considered in the damping unit of the viscoelastic boundary, and the reflection phenomenon on the boundary is eliminated. However, the spring element more accurately simulates the elastic recovery property of semi-infinite soil. The viscoelastic boundary is convenient to apply, has been preliminarily realized in large-scale general finite element software, and can meet the requirements of engineering accuracy (Liu et al. 2005). Hence, the viscoelastic artificial boundary technique has been increasingly applied in research and engineering problems (Liu et al. 2002; Zhou et al. 2005; Pan et al. 2005). The normal and tangential spring stiffness and damping coefficient of viscoelastic artificial boundaries can be obtained by the following formulas.

$$K_{BN} = \alpha_N \frac{G}{R}, \quad C_{BN} = \rho c_p \quad (11)$$

$$K_{BT} = \alpha_T \frac{G}{R}, \quad C_{BT} = \rho c_s \quad (12)$$

where K_{BN} and K_{BT} represent the elastic stiffness and tangential spring stiffness, respectively; R is the distance from the wave source to the artificial boundary point; c_p and c_s are the speed of P wave

and speed of S wave of the medium, respectively; G is the shear modulus of the medium; ρ is the medium density; and α_N and α_T are correction coefficients. In general, α_N is 0.8–1.2, and α_T is 0.35–0.65; in this paper, α_N is 1.0, and α_T is 0.5.

In this paper, loess from Taiyuan is selected as the analysis object. The relationship between the dynamic parameters and the moisture content is presented in the existing literature (Wang et al. 2012). Considering the seismic response of loess tunnels with different moisture contents and using Eqs. (11)–(12), the normal and tangential spring stiffness and damping coefficients of the viscoelastic artificial boundary are obtained for different moisture contents. The calculation results are shown in Table 1.

3.2 Seismic Wave

In this paper, the Imperial Valley El-Centro earthquake wave (north–south component; magnitude M = 6.7; epicentral distance, 9.3 km; maximum acceleration, 2.49 m/s^2), which occurred in the United States in 1940, is used for the dynamic analysis. This earthquake wave was the first to be recorded and is of great significance in seismic research. With consideration of the difference between the seismic amplitude of the original earthquake amplitude and the seismic amplitude required in the dynamic response analysis, the peak is adjusted to 2.20 m/s^2 according to relative standards (Code for seismic design of buildings (GB 50011-2010), which is equivalent to a rare seismic fortification intensity of 7. The El-Centro wave is input from the bottom of the tunnel model in the horizontal direction to analyze the seismic response.

4 The Seismic Stability of the Tunnel Considering the Dynamic Parameters of Loess

4.1 Calculation Model

In this paper, the dynamic finite element static strength reduction method is used to analyze the stability of a loess tunnel subjected to an earthquake. A two-dimensional plane model is established according to the literature (Fang 2005) using a 1 m thickness from the semi-infinite space of the loess mass surrounding the tunnel.

In this paper, the tunnel model has an original span of 12 m and a height of 8 m, and the initial lining and secondary lining are concrete with thicknesses of 0.30 and 0.50 m, respectively. Considering the reserve problems of loess mass strength and efficiency in the numerical simulation, the semi-infinite space is set to 40 m from the tunnel bottom, which is 5 times the height of the cavern, and the left and right sides of the tunnel are extended to 60 m, which is 5 times the cavern span.

When using the dynamic finite element static strength reduction method, the seismic response

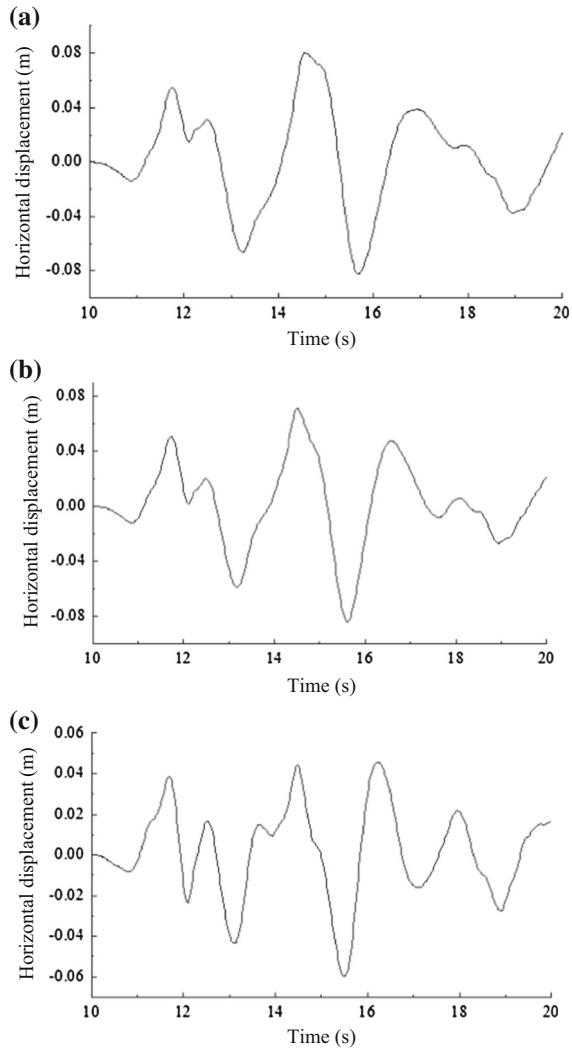

Fig. 1 Horizontal displacement–time history curve of nodes 1940, 2018 and 2070. **a** Node 1940, **b** node 2018, **c** node 2070

Table 2 Horizontal displacement of node 1940 from 14 to 15 s

Time (s)	Displacement (m)	Time (s)	Displacement (m)	Time (s)	Displacement (m)	Time (s)	Displacement (m)
14	− 8.183E−3	14.26	3.017E−2	14.52	7.916E−2	14.78	7.304E−2
14.02	− 5.431E−3	14.28	3.420E−2	14.54	7.995E−2	14.8	7.227E−2
14.04	− 2.654E−3	14.3	3.854E−2	**14.56**	**8.022E−2**	14.82	7.180E−2
14.06	1.446E−4	14.32	4.317E−2	14.58	8.009E−2	14.84	7.168E−2
14.08	2.917E−3	14.34	4.805E−2	14.6	7.967E−2	14.86	7.169E−2
14.1	5.646E−3	14.36	5.294E−2	14.62	7.908E−2	14.88	7.144E−2
14.12	8.360E−3	14.38	5.756E−2	14.64	7.845E−2	14.9	7.082E−2
14.14	1.109E−2	14.4	6.186E−2	14.66	7.791E−2	14.92	6.987E−2
14.16	1.388E−2	14.42	6.590E−2	14.68	7.743E−2	14.94	6.866E−2
14.18	1.677E−2	14.44	6.965E−2	14.7	7.681E−2	14.96	6.719E−2
14.2	1.979E−2	14.46	7.298E−2	14.72	7.598E−2	14.98	6.537E−2
14.22	2.300E−2	14.48	7.572E−2	14.74	7.501E−2	15	6.307E−2
14.24	2.645E−2	14.5	7.778E−2	14.76	7.399E−2	–	–

Bold indicates maximum value

Table 3 Horizontal displacement of the boundary nodes at 14.56 s

Node	Displacement (m)	Node	Displacement (m)	Node	Displacement (m)	Node	Displacement (m)
1844	7.648E−2	706	5.772E−2	1940	8.022E−2	1118	4.560E−2
1890	7.646E−2	722	5.732E−2	1955	8.030E−2	1133	3.973E−2
129	7.502E−2	738	5.677E−2	369	7.896E−2	1148	3.363E−2
530	7.467E−2	754	5.590E−2	385	7.876E−2	1163	2.753E−2
546	7.331E−2	770	5.495E−2	401	7.762E−2	1178	2.123E−2
562	7.180E−2	786	5.333E−2	417	7.625E−2	1193	1.538E−2
578	7.009E−2	802	5.143E−2	433	7.457E−2	1208	9.610E−3
594	6.823E−2	818	4.863E−2	449	7.264E−2	1223	4.596E−3
610	6.627E−2	834	4.508E−2	465	7.035E−2	1238	2.429E−4
626	6.424E−2	850	4.083E−2	481	6.769E−2	1253	− 3.492E−3
642	6.218E−2	866	3.521E−2	497	6.454E−2	1268	− 5.837E−3
658	6.020E−2	882	2.784E−2	513	6.088E−2	1283	− 6.777E−3
674	5.827E−2	898	1.878E−2	529	5.576E−2	1298	− 5.643E−3
690	5.814E−2	914	0	1103	5.113E−2	1313	0

analysis of the dynamic model must be conducted. Then, the displacement–time curve of model in the right corner node is chosen. To determine when the maximum displacement moment occurs, all horizontal displacements of the model boundary nodes corresponding to each moment are extracted and input into the static model of the loess tunnel. The shear strength parameters of the loess mass surrounding the tunnel are constantly reduced until the calculation does not converge; at this point, the reduction factor is the safety factor.

4.2 Seismic Stability of a loess Tunnel Under Different Moisture Contents

4.2.1 Moisture Content: 5%

The horizontal displacement–time history curves in the upper right corner node of the model are

Table 4 Nephogram of the plastic strain and safety factor

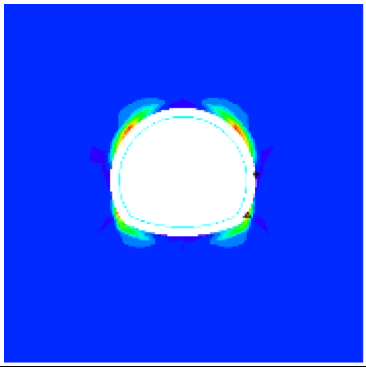

a. Loess cover thickness: 13.2 m

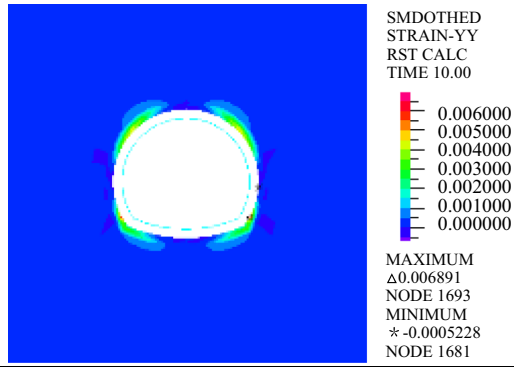

b. Loess cover thickness: 19.8 m

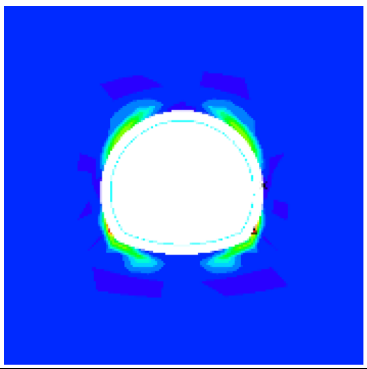

c. Loess cover thickness: 26.4 m

S a. η =2.256

b. η =2.312

c. η =2.407

Safety factor

investigated for loess cover thicknesses of 13.2, 19.8 and 26.4 m, corresponding to nodes 1940, 2018, and 2070, respectively. The horizontal displacement–time history curves of the three nodes are illustrated as follows.

In Fig. 1, the displacement peak of node 1940 occurs between 14 and 15 s. The horizontal displacements of node 1940 are extracted between 14 and 15 s and are listed in Table 2.

In Table 2, at 14.56 s, the horizontal displacement of node 1940 reaches the maximum value of 8.022E−2m. The horizontal displacements of all nodes on both sides of the vertical boundary of the dynamic model have also been obtained at 14.56 s, as shown in Table 3.

The horizontal displacements of all boundary nodes, which are regarded as the initial displacements, are input into the static model, and the dynamic finite

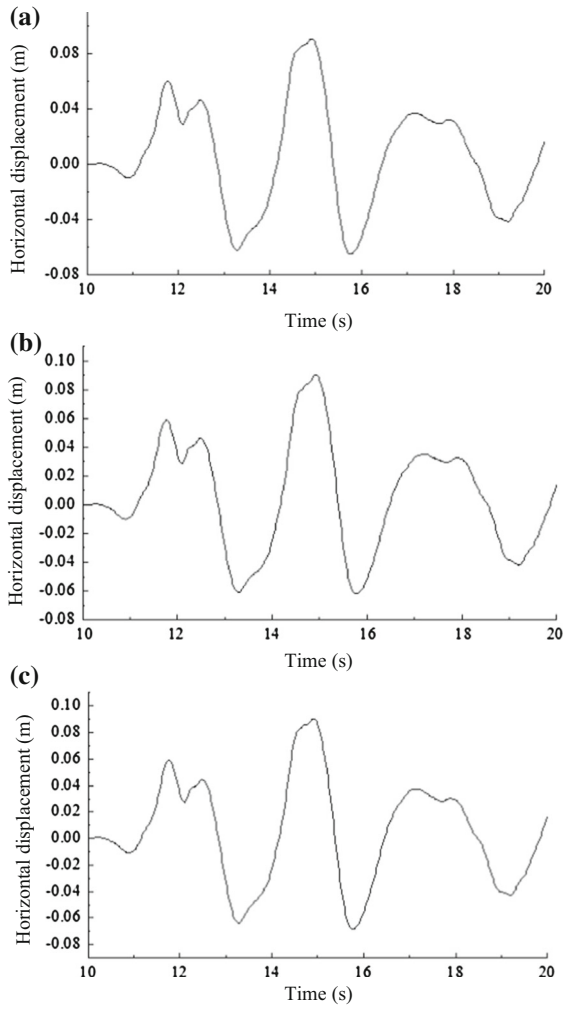

Fig. 2 Horizontal displacement–time curves of nodes 1940, 2018 and 2070. **a** Node 1940, **b** node 2018, **c** node 2070

element static strength reduction method is used to analyze the seismic stability of the loess tunnel.

The same method can be used for the loess cover thickness of 19.8 m, in which the maximum horizontal displacement occurs at 14.52 s, and for the loess cover thickness of 26.4 m, in which the maximum horizontal displacement occurs at 14.48 s.

By using the dynamic finite element static strength reduction method and reducing the dynamic parameters of the loess mass until the model calculation does not converge, the safety factor and plastic zone distribution of the tunnel are obtained for a moisture content of 5% and loess cover thicknesses of 13.2, 19.8 and 26.4 m, as shown in Table 4.

In Table 4, the plastic zone first occurs in the arch feet and arch shoulders, and a plastic zone does not appear in the vault, which is more secure. With increasing loess cover thickness from 13.2 to 19.8 to 26.4 m, the plastic area spreads gradually from the lining to the rock mass. The safety factors are 2.256, 2.312 and 2.407, respectively, and the safety factors increase with increasing loess cover thickness.

4.2.2 Moisture Content: 10%

The horizontal displacement–time history curves in the upper right corner node of the model are again chosen for loess cover thicknesses of 13.2, 19.8 and 26.4 m. The horizontal displacement–time history curves of three different nodes are illustrated in Fig. 2.

The horizontal displacement reaches the maximum at 14.92 s when the loess cover thickness is 13.2 m, at 14.92 s when the loess cover thickness is 19.8 m, and at 14.90 s when the loess cover thickness is 26.4 m. The displacement peak of node 1940 occurs between 14 and 15 s. When the maximum displacement occurs, the horizontal displacements of the two lateral boundary nodes are input, and the dynamic finite element static strength reduction method is used.

By reducing the parameters of the loess mass until the model calculation does not converge, the safety factor and plastic zone distribution are obtained, as shown in Table 5.

In Table 5, the plastic zones first occur in the arch feet and arch shoulders on both sides of the tunnel. With increasing loess cover thickness from 13.2 to 19.8 to 26.4 m, the plastic zone increases but varies little and gradually shifts from the lining to the rock mass. The safety factors are 2.196, 2.280 and 2.328 for the loess cover thicknesses of 13.2, 19.8 and 26.4 m, respectively.

Table 5 Plastic strain nephogram and safety factor

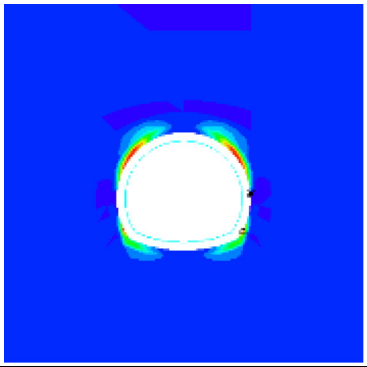

a. Loess cover thickness: 13.2 m

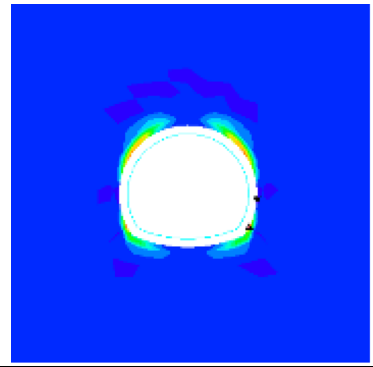

b. Loess cover thickness: 19.8 m

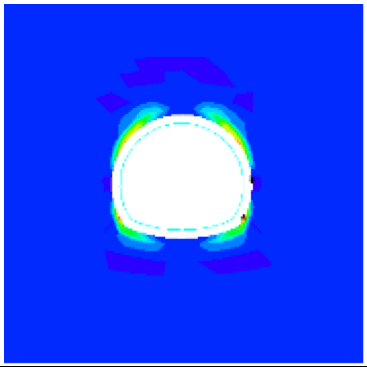

c. Loess cover thickness: 26.4 m

a. η=2.196

b. η=2.280

c. η=2.328

Safety factor

4.2.3 Moisture Content: 15%

The horizontal displacement–time history curves in the upper right corner node of the model are chosen for loess cover thicknesses of 13.2, 19.8 and 26.4 m, corresponding to nodes 1940, 2018, and 2070, respectively. The horizontal displacement–time history curves of the three nodes are illustrated in Fig. 3.

In the analysis, the horizontal displacement reaches the maximum at 15.00 s for the loess cover thickness of 13.2 m, at 15.00 s for the loess cover thickness of 19.8 m, and at 15.02 s for the loess cover thickness of 26.4 m. The displacement peak of node 1940 occurs between 14 and 15 s. The horizontal displacements of the two lateral boundary nodes at the point of maximum displacement are input, and the dynamic finite element static strength reduction method is used.

By reducing the dynamic parameters of the loess mass until the model calculation does not converge, the safety factor and plastic zone distribution of the tunnel are obtained, as shown in Table 6.

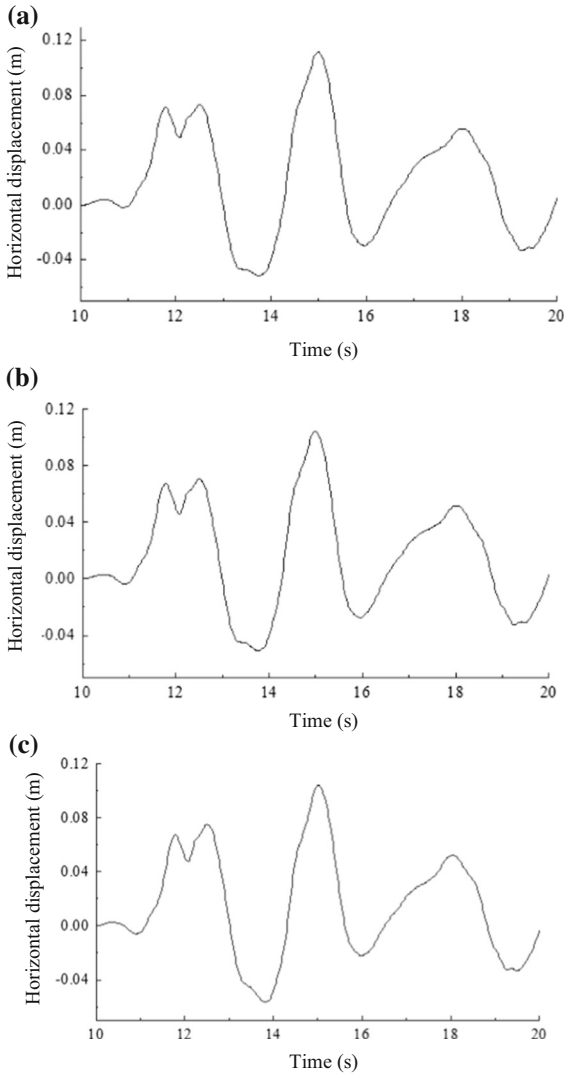

Fig. 3 Horizontal displacement–time history curve of nodes 1940, 2018 and 2070. **a** Node 1940, **b** node 2018, **c** node 2070

From Table 6, the plastic zones first occur in the arch feet and arch shoulders on both sides of the tunnel. As the loess cover thickness increases from 13.2 to 19.8 to 26.4 m, the plastic zone develops in the lining, and the safety factors are 1.994, 2.055 and 2.227, respectively.

4.3 Dynamic Stability of the Loess Tunnel Under Conditions of Different Vibration Durations

According to the literature (Zienkiewicz et al. 1975), in dynamic intensity testing, different vibration durations correspond to different seismic fortification intensities; specifically, vibration durations of 10, 20 and 30 cycles correspond to rare seismic fortification intensities of 7, 7.5 and 8. The stability of a tunnel in loess with a moisture content of 10% is analyzed here.

4.3.1 Calculation Parameters and Seismic Wave

In the analysis, the dynamic internal friction angle of the loess is not affected by the vibration duration. Dynamic cohesion maintains a linear relation with the vibration duration and decreases continuously with increasing vibration duration, and the elastic modulus and Poisson's ratio have no effect on stability. Therefore, a tunnel in loess with a moisture content of 15% is chosen for the stability analysis, as shown in Table 7.

For a vibration duration of 10 cycles, the maximum dynamic elastic modulus is the same, as shown in Table 3. The El-Centro wave is also used in this analysis. Because the original seismic amplitude and the seismic amplitude needed for dynamic stability analysis are not consistent, the peak is adjusted to 3.0 m/s^2 according to the relative standards, which is equivalent to a rare seismic fortification intensity of 7.5, and to 3.80 m/s^2, which is equivalent to a rare seismic fortification intensity of 8. To consider the horizontal seismic action, the El-Centro wave is input from the bottom of the tunnel model.

4.3.2 Vibration Duration: 20 Cycles

The horizontal displacement–time history curves of the upper right corner are analyzed for loess cover thicknesses of 13.2, 19.8 and 26.4 m, corresponding to nodes 1940, 2018, and 2070, respectively. The horizontal displacement–time history curves of the three nodes are illustrated in Fig. 4.

Table 6 Plastic strain nephogram and safety factor

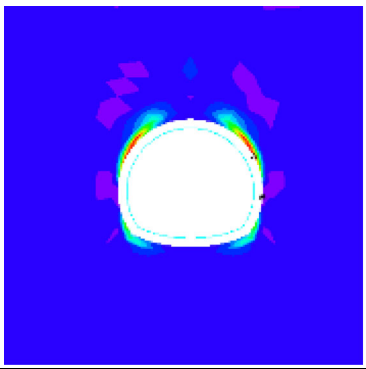

a. Loess cover thickness: 13.2 m

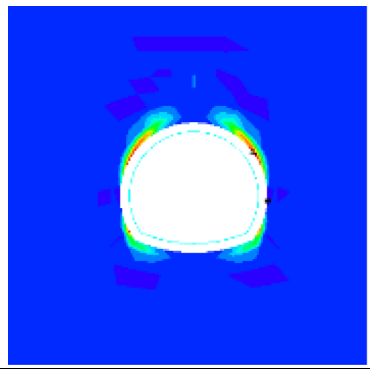

b. Loess cover thickness: 19.8 m

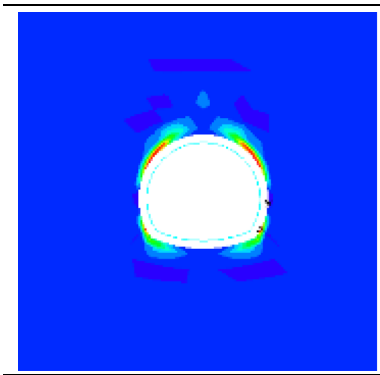

c. Loess cover thickness: 26.4 m

a. η =1.994

b. η =2.055

c. η =2.227

Safety factor

In Fig. 4, the displacement peak of node 1940 occurs between 14 and 15 s; hence, the horizontal displacements of node 1940 are extracted between 14 and 15 s and are shown in Table 8.

In Table 8, at 14.92 s, the horizontal displacement of node 1940 reaches the maximum value of 1.214E−1m. The horizontal displacements of all nodes on both sides of the vertical boundary of the dynamic model are thus obtained at 14.92 s and are shown in Table 9.

The horizontal displacements of all boundary nodes, which are regarded as the initial displacements, are input. When the loess cover thickness is 19.8 m, the maximum horizontal displacement occurs at 14.92 s, and when the loess cover thickness is 26.4 m, the maximum horizontal displacement occurs at 14.90 s.

Table 7 Material physical mechanical parameters

Material	Maximum dynamic elastic modulus (GPa)	Poisson's ratio	Volume-weight (kN/m^3)	Dynamic cohesive force (kPa)	Internal friction angle (°)
Loess (vibration duration: 20 cycles)	–	0.35	14.08	20.8	24.6
Loess (vibration duration: 30 cycles)	–	0.35	14.08	18.4	24.6

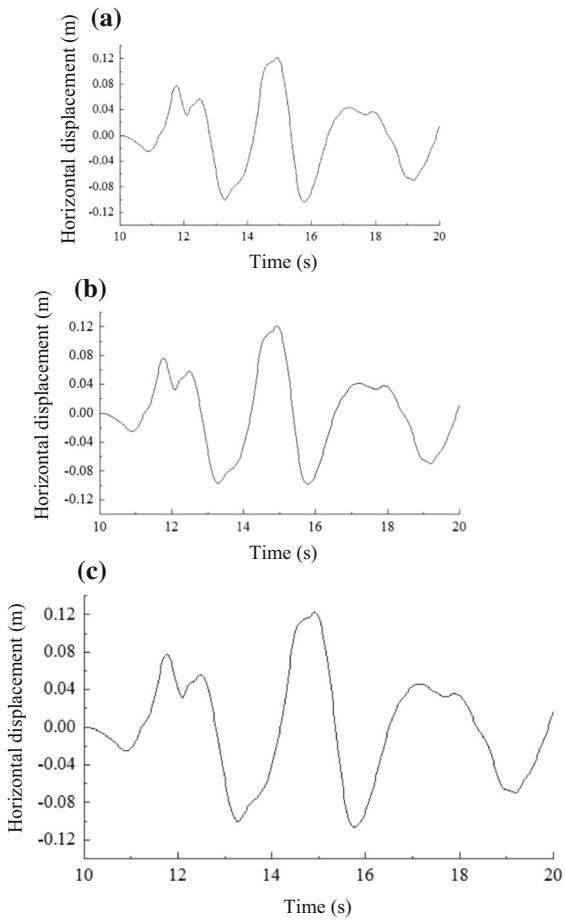

Fig. 4 Horizontal displacement–time history curve of nodes 1940, 2018 and 2070. **a** Node 1940, **b** node 2018, **c** node 2070

By reducing the dynamic parameters of the loess mass until the model calculation does not converge, the safety factor and plastic zone distribution of the tunnel are obtained for a rare seismic fortification intensity of 7.5 in conjunction with loess cover thicknesses of 13.2, 19.8 and 26.4 m, as shown in Table 10.

In Table 10, the plastic zones first form in the arch feet and arch shoulders on both sides of the tunnel. The loess cover thicknesses of 13.2, 19.8 and 26.4 m result in safety factors of 2.256, 2.312 and 2.407, respectively, and the safety factors increase with increasing loess cover thickness.

4.3.3 Vibration Duration: 30 Cycles

The horizontal displacement–time history curves in the upper right corner node of the model are analyzed for loess cover thicknesses of 13.2, 19.8 and 26.4 m, corresponding to nodes 1940, 2018, and 2070, respectively. The horizontal displacement–time history curves of the three nodes are illustrated in Fig. 5.

The horizontal displacement reaches the maximum at 14.92 s when the loess cover thickness is 13.2 m, at 14.92 s when the loess cover thickness is 19.8 m, and at 14.90 s when the loess cover thickness is 26.4 m. The horizontal displacements of the two lateral boundary nodes corresponding to the time of the maximum displacement are input, and the dynamic finite element static strength reduction method is used.

By reducing the dynamic parameters of the loess mass until the model calculation does not converge, the safety factor and plastic zone distribution of the loess tunnel are obtained for loess cover thicknesses of 13.2, 19.8 and 26.4 m, as shown in Table 11.

According to Table 11, the plastic zones first occur in the arch feet and arch shoulders on both sides of the tunnel. For loess cover thicknesses of 13.2, 19.8 and 26.4 m, the safety factors are 2.196, 2.280 and 2.328, respectively.

Table 8 Horizontal displacements of boundary node 1940 from 14 to 15 s

Time (s)	Displacement (m)	Time (s)	Displacement (m)	Time (s)	Displacement (m)	Time (s)	Displacement (m)
14	− 4.251E−2	14.26	1.800E−2	14.52	1.028E−1	14.78	1.153E−1
14.02	− 3.843E−2	14.28	2.457E−2	14.54	1.054E−1	14.8	1.158E−1
14.04	− 3.426E−2	14.3	3.166E−2	14.56	1.073E−1	14.82	1.167E−1
14.06	− 3.003E−2	14.32	3.294E−2	14.58	1.087E−1	14.84	1.181E−1
14.08	− 2.579E−2	14.34	4.721E−2	14.6	1.096E−1	14.86	1.197E−1
14.1	− 2.156E−2	14.36	5.526E−2	14.62	1.104E−1	14.88	1.208E−1
14.12	− 1.731E−2	14.38	6.296E−2	14.64	1.112E−1	14.9	1.213E−1
14.14	− 1.298E−2	14.4	7.025E−2	14.66	1.121E−1	14.92	1.214E−1
14.16	− 8.524E−3	14.42	7.723E−2	14.68	1.131E−1	14.94	1.209E−1
14.18	− 3.871E−3	14.44	8.383E−2	14.7	1.139E−1	14.96	1.201E−1
14.2	1.041E−3	14.46	8.986E−2	14.72	1.145E−1	14.98	1.187E−1
14.22	6.277E−3	14.48	9.513E−2	14.74	1.148E−1	15	1.166E−1
14.24	1.190E−2	14.5	9.944E−2	14.76	1.150E−1	–	–

Table 9 Horizontal displacements of the boundary nodes at 14.92 s

Node	Displacement (m)	Node	Displacement (m)	Node	Displacement (m)	Node	Displacement (m)
1844	1.212E−1	706	7.682E−2	1940	1.214E−1	1118	7.687E−2
1890	1.207E−1	722	7.251E−2	1955	1.208E−1	1133	7.255E−2
129	1.181E−1	738	6.800E−2	369	1.183E−1	1148	6.803E−2
530	1.170E−1	754	6.333E−2	385	1.172E−1	1163	6.335E−2
546	1.145E−1	770	5.849E−2	401	1.147E−1	1178	5.850E−2
562	1.117E−1	786	5.347E−2	417	1.119E−1	1193	5.348E−2
578	1.087E−1	802	4.827E−2	433	1.088E−1	1208	4.828E−2
594	1.053E−1	818	4.286E−2	449	1.055E−1	1223	4.287E−2
610	1.018E−1	834	3.724E−2	465	1.019E−1	1238	3.725E−2
626	9.795E−2	850	3.134E−2	481	9.804E−2	1253	3.135E−2
642	9.387E−2	866	2.518E−2	497	9.395E−2	1268	2.519E−2
658	8.959E−2	882	1.838E−2	513	8.966E−2	1283	1.839E−2
674	8.445E−2	898	1.154E−2	529	8.451E−2	1298	1.155E−2
690	8.100E−2	914	0	1103	8.105E−2	1313	0

4.4 Results Analysis

The dynamic parameters of loess with different moisture contents and different vibration durations are considered, and the dynamic finite element static strength reduction method is utilized. By analyzing the seismic stability of loess tunnels with different loess cover thicknesses, different moisture contents and different vibration durations, the safety coefficients of loess tunnels in the critical state under earthquake conditions are obtained. The analysis results are summarized in Fig. 6.

Table 10 Nephogram of the plastic strain and safety factor

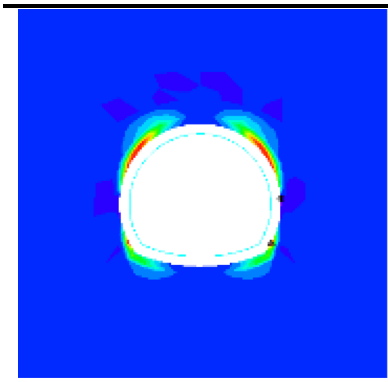

a. Loess cover thickness: 13.2 m

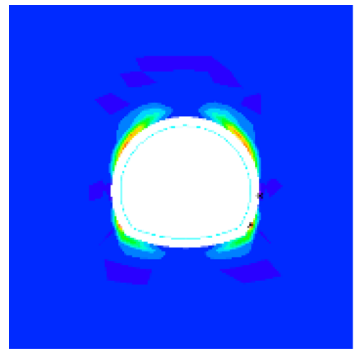

b. Loess cover thickness: 19.8 m

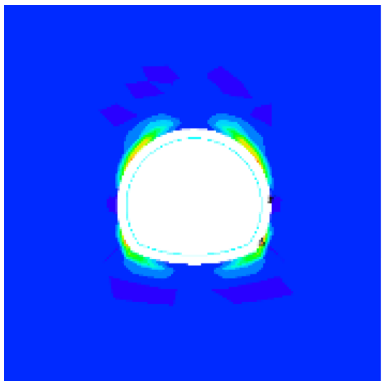

c. Loess cover thickness: 26.4 m

a. η =2.141

b. η =2.251

c. η =2.309

Safety factor

According to Fig. 6a, for a given loess cover thickness, lower loess moisture contents are associated with higher safety coefficients. In addition, the safety coefficient increases with increasing loess cover thickness. When the loess cover thickness increases from 13.2 to 26.4 m, the safety coefficient increases by approximately 0.15 at a loess moisture content of 5%, by approximately 0.13 at a loess moisture content of 10%, and by approximately 0.23 at a loess moisture content of 15%. Hence, greater loess cover thicknesses produce higher safety coefficients.

From Fig. 6b, for a given loess cover thickness, shorter vibration durations (corresponding to seismic fortification intensity) correspond to larger safety coefficients for loess tunnels. In addition, with increasing loess cover thickness, the safety coefficient

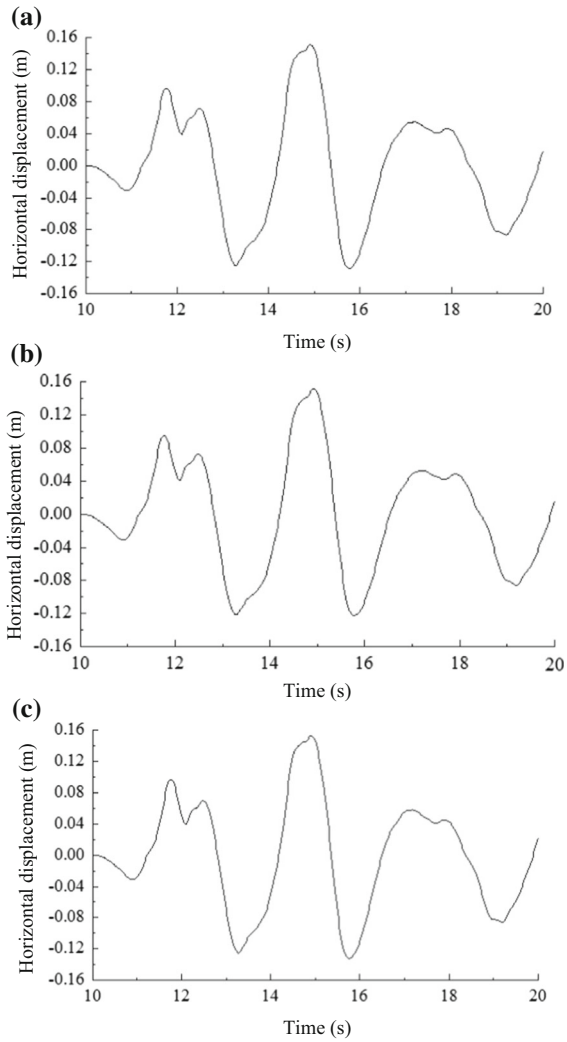

Fig. 5 Horizontal displacement–time history curve of nodes 1940, 2018 and 2070. **a** Node 1940, **b** node 2018, **c** node 2070

increases. When the loess cover thickness increases from 13.2 to 26.4 m, the safety coefficient increases by approximately 0.13 for a vibration duration of 10 cycles, by approximately 0.16 for a vibration duration of 15 cycles, and by approximately 0.17 for a vibration duration of 20 cycles. The thicker the loess cover is, the safer the tunnel is.

Therefore, lower moisture contents, shorter vibration durations (corresponding to the seismic fortification intensity), and greater loess cover thicknesses result in larger safety factor values, which indicate that the loess tunnel is safer. When the loess moisture content increases from 5 to 15%, the safety coefficient decreases by approximately 0.26 for a loess cover thickness of 13.2 m, by approximately 0.31 for a loess cover thickness of 19.8 m, and by approximately 0.18 for a loess cover thickness of 26.4 m. When the vibration duration increases from 10 to 30 cycles, the safety coefficient decreases by approximately 0.13 for a loess cover thickness of 13.2 m, by approximately 0.08 for a loess cover thickness of 19.8 m, and by approximately 0.12 for a loess cover thickness of 26.4 m. The safety coefficient increases as the loess cover thickness increases.

5 Conclusions

1. In response to an earthquake, the plastic zone in a loess tunnel in the critical state develops in the arch feet and the arch shoulders.
2. With increasing loess cover thickness, the plastic zone of the tunnel gradually shifts from the lining to the loess mass, indicating that the loess tunnel becomes safer with increasing depth.
3. For a given loess cover thickness, lower loess moisture contents are associated with higher loess tunnel safety coefficients and, thus, safer tunnels.
4. Greater loess cover thicknesses yield higher loess tunnel safety coefficients and, thus, safer tunnels.

Table 11 Nephogram of the plastic strain and safety factor

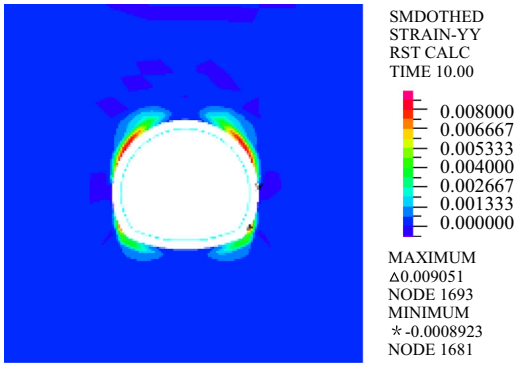	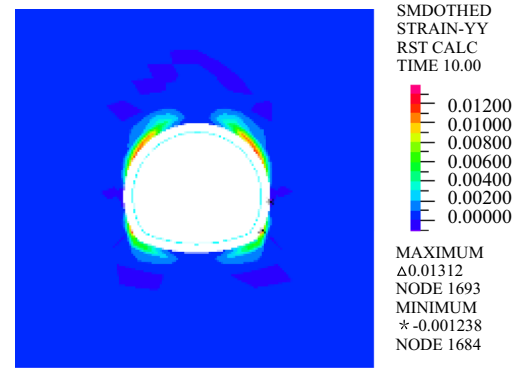
a. Loess cover thickness: 13.2 m	**b. Loess cover thickness: 19.8 m**
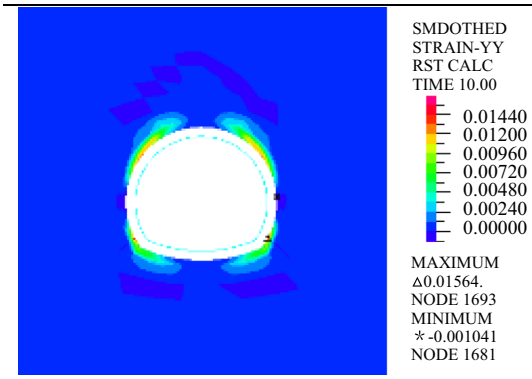	a. η =2.124 b. η =2.234 c. η =2.292
c. Loess cover thickness: 26.4 m	**Safety factor**

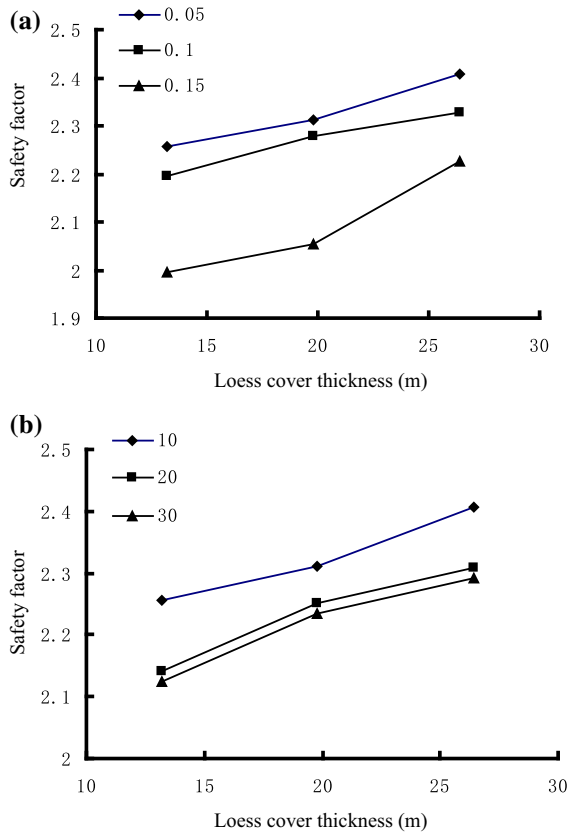

Fig. 6 Safety factors for loess tunnels with different water contents and under different earthquakes conditions. **a** Safety factor with different water contents: 0.05, 0.1, 0.15 stand for water content 5, 10 and 15%, respectively. **b** Safety factor under different earthquake conditions: 10, 20 30 stand for rare seismic fortification intensities 7, 7.5 and 8, respectively

5. Lower seismic fortification intensity values or shorter vibration durations yield higher loess tunnel safety coefficients and, thus, safer tunnels.

Acknowledgements This paper is a part of the National Natural Science Foundation of China (Grant number: 51478212), and and a part of science and technology project in the Zhejiang Traffic Quality Supervision Bureau (Grant number: ZJ201602), and a part of science and technology project in China Railway 12th Bureau Group (Grant number: 14B-3).

Compliance with Ethical Standards

Conflict of interest The authors declare that there is no conflict of interests regarding the publication of this paper.

References

Chen LW, Peng JB, Fan W (2007) Stability of loess-hidden hole under earthquake. J Chang'an Univ Nat Sci Edn 27(6):34–36

Chen SY, Li Z, Zhang TY et al (2011) Acceleration discrimination of stability and reliability analysis of surrounding rock of loess tunnel. Appl Mech Mater 105–107:1555–1560

Cheng XS, Zheng YR (2011) Calculation discussion about safety factor of unlined loess tunnel wall rock structure under earthquake. Rock Soil Mech 3:761–766

Cheng XS, Zhu HY, Tian RR et al. (2010) Soil mass stability analysis of circular unlined loess tunnel under earthquake action. In: International symposium on geo mechanics and geo technics: From Micro to Macro, pp 1127–1134

Cheng XS, Zheng YR, Tian RR (2011a) Dynamic finite element strength reduction method of earthquake stability analysis of surrounding rock of tunnel. Rock Soil Mech 32(4):1241–1248

Cheng XS, Tian RR, Zheng YR (2011b) Earthquake stability analysis of wall rock of vertical ridge loess tunnel—the impact of stress concentration at tunnel feet on safety factor. J Vib Shock 30(11): 214–216 + 218 +223

Cheng XS, Shi W, Tian RR (2014) Safety assessment of lined loess tunnel under earthquake. Electron J Geotech Eng 19(I):1903–1915

Cheng XS, Feng H, Qi S et al (2017) Dynamic response of curved wall LTSLS under the interaction of rainwater seepage and earthquake. Geotech Geol Eng 35(3):1–12

Code for seismic design of buildings (GB 50011-2010). Beijing: China Architecture & Building Press, 2016

Dawson EM, Roth WH, Drescher A (1999) Slope stability analysis by strength reduction. Geo-technique 49(6):835–840

Fang YG (2005) Theory and application of dynamic interaction between soil and rock. Science Press, Shanghai, pp 66–69

Griffiths DV, Lane PA (1999) Slope stability analysis by finite elements. Geo-technique 49(3):387–403

Guo J, Wang QC (2011) The numerical simulation analysis of excavation process of loess tunnel. Adv Mater Res 383–390:6594–6600

Li XA, Li RJ, Che GF et al (2011) On the stability of unsaturated loess slope under tunneling condition. Adv Mater Res 233–235:2678–2681

Liu JB, Wang ZY, Zhang KF et al (2002) 3D finte element analysis of large dynamic machine foundation considering soil-structure interaction. Eng Mech 19(3):34–38

Liu JB, Wang ZY, Du XL et al (2005) Three-dimensional visco-elastic artificial boundaries in time domain for wave motion problems. Eng Mech 22(6):46–51

Liu FB, Wu SC, Li J et al (2012) Study on optimum multi-parameter growth functions of deformation prediction for loess tunnel initial structure. Appl Mech Mater 170–173:1769–1772

Pan DG, Lou ML, Dong C (2005) Seismic response analysis of soil layer under uniform excitation. Chin J Comput Mech 22(5):562–567

Peila D (1994) A theoretical study of rein for cement influence on the stability of a tunnel face. Geotech Geol Eng 12:145–168

Peng JB, Li QC, Chen ZX (2008) Loess cave hazards. Science Press, Beijing, pp 232–253

Qiu CY, Zheng YR, Song YK (2009) Exploring the safety factors of unlined loess tunnel by ANSYS. Chin J Undergr Space Eng 5(2):291–296

Soranzo E, Wu W, Tamagnini R (2015) Face stability of shallow tunnels in partially saturated soil: centrifuge testing and numerical analysis. Géotechnique 65(6):454–467

Wang J, Shi YC, Wang Q et al (2012) Study on dynamic strength properties of undisturbed loess under natural moisture content. World Earthq Eng 8(4):23–27

Xu ZH (2005) Qualitative estimation method for stability of tunnels in seismic regions. Technol Highw Transp 3:152–155

Yang MJ, Chang XD The excavation procedure of super-large underground chambers and the surrounding rock stability. Journal of Southwest Jiao Tong University, 2000 2, 35(1): 32–35

Zhang LM, Zheng YR, Wang ZQ et al (2007) Application of strength reduction finite element method to road tunnels. Rock Soil Mech 28(1):97–106

Zhang H, Zheng YR, Yang Z et al (2009) Exploration of safety factors of the loess tunnel. Chin J Undergr Space Eng 5(2):297–306

Zhang JH, Yang XL, Zhang B (2015) Upper bound qusai-static analysis of dynamic stability on shallow tunnel under earthquake action. J Cent South Univ Sci Technol 1:238–247

Zheng YR, Zhao SY, Zhang LY (2002) Slope stability analysis by strength reduction FEM. Eng Sci 4(10):57–62

Zheng YR, Qiu CY, Zhang H (2008) Exploration of stability analysis methods for surrounding rocks of soil tunnel. Chin J Rock Mech Eng 27(10):1968–1980

Zheng YR, Xiao Q, Ye HL et al (2010a) Study of tunnel stability analysis with seismic load. Chin J Rock Mech Eng 29(6):1081–1088

Zheng YR, Ye HL, Xiao Q et al (2010b) Analysis of seismic slope and tunnel stability based on full dynamic analysis. J Disaster Prev Mitig Eng 30(S1):279–285

Zhou J, Bai B, Xu JP (2001) Theory and calculation of soil dynamics. China Architecture & Building Press, Beijing

Zhou AH, Zhang HR, Yuan Y et al (2005) Effect analysis of composite foundation parameters on ground dynamic characteristics. China Saf Sci J 15(11):3–6

Zienkiewicz OC, Humpheson C, Lewis RW (1975) Associated and non-asociated visco-plasticity and plasticity in soil mechanics. Geo Technique 25(4):671–689